Capillary interfacial tension in active phase separation

G. Fausti,[1] E. Tjhung,[2] M. E. Cates,[3] and C. Nardini[1,4]

[1]*Service de Physique de l'Etat Condensé, CEA, CNRS Université Paris-Saclay, CEA-Saclay, 91191 Gif-sur-Yvette, France*
[2]*Department of Physics, University of Durham, Science Laboratories, South Road, Durham DH1 3LE, UK*
[3]*DAMTP, Centre for Mathematical Sciences, University of Cambridge, Wilberforce Road, Cambridge CB3 0WA, UK*
[4]*Sorbonne Université, CNRS, Laboratoire de Physique Théorique de la Matière Condensée, 75005 Paris, France*
(Dated: May 25, 2021)

In passive fluid-fluid phase separation, a single interfacial tension sets both the capillary fluctuations of the interface and the rate of Ostwald ripening. We show that these phenomena are governed by two different tensions in active systems, and compute the capillary tension σ_{cw} which sets the relaxation rate of interfacial fluctuations in accordance with capillary wave theory. We discover that strong enough activity can cause negative σ_{cw}. In this regime, depending on the global composition, the system self-organizes, either into a microphase-separated state in which coalescence is highly inhibited, or into an 'active foam' state. Our results are obtained for Active Model B+, a minimal continuum model which, although generic, admits significant analytical progress.

Active particles extract energy from the environment and dissipate it to self-propel [1, 2]. One of their notable self-organizing features is phase separation into dense (liquid) and dilute (vapor) regions, happening even for purely repulsive particles [3–5]. Although generically a far-from-equilibrium effect, active phase separation was first described via an approximate mapping onto equilibrium liquid-vapor phase separation [3, 4]. This led to early speculation that time reversal symmetry might be restored macroscopically in steady state [3, 6–11]. Indeed, activity is an irrelevant perturbation near the liquid-vapor critical point, albeit without leading to emergent reversibility [12].

Recently it has become clear, however, that bulk phase separation in active systems displays strongly non-equilibrium features. Bubbly phase separation [13] was evidenced in simulations of repulsive self-propelled particles [14, 15]: here large liquid droplets contain a population of mesoscopic vapor bubbles that are continuously created in the bulk, coarsen, and are ejected into the exterior vapor, thereby creating a circulating phase-space current in the steady state. Microphase separation of vapor bubbles [15, 16] has been further observed numerically, whereas a similar phase of finite dense clusters is often found in experiments with self-propelled colloids [17, 18] and bacteria [19]. Recently, even more intriguing forms of phase separation have been reported in an active system composed of nematodes [20].

Much understanding of the physics of active phase separation has been gained from continuum field theories. In the simplest setting [13, 21, 22], these only retain the evolution of the density field ϕ, while hydrodynamic [23, 24] or polar [25] fields can be added if the phenomenology requires. Their construction, via conservation laws and symmetry arguments, follows a path first introduced with Model B for passive phase separation [26–28]. Yet, these field theories differ from Model B because locally broken time-reversal symmetry implies that new non-linear terms are allowed. The ensuing minimal self-consistent

theory, Active Model B+ (AMB+) [11, 13] includes all terms that break detailed balance up to order $\mathcal{O}(\nabla^4\phi^2)$ in a gradient expansion [11, 13] and is defined by

$$\partial_t \phi = -\nabla \cdot \left(\mathbf{J} + \sqrt{2DM}\mathbf{\Lambda} \right) \tag{1}$$

$$\mathbf{J}/M = -\nabla\mu_\lambda + \zeta(\nabla^2\phi)\nabla\phi \tag{2}$$

$$\mu_\lambda[\phi] = \frac{\delta\mathcal{F}}{\delta\phi} + \lambda|\nabla\phi|^2 \tag{3}$$

where $\mathcal{F} = \int d\mathbf{r} \left[f(\phi) + \frac{K(\phi)}{2}|\nabla\phi|^2 \right]$, $f(\phi)$ is a double-well local free energy, and $\mathbf{\Lambda}$ is a vector of zero-mean Gaussian white noises with unit variance. Model B is recovered at vanishing activity ($\lambda = \zeta = 0$), unit mobility ($M = 1$) and constant noise level D [26].

It is known that at low activity (small λ, ζ), AMB+ undergoes conventional bulk phase separation. At higher activity, Ostwald ripening [29], the classical diffusive pathway to macroscopic phase separation, can be thrown into reverse [13]. This explains the emergence of bubbly phase separation and microphase-separated vapor bubbles. (These phases arise when $\zeta, \lambda > 0$; for $\zeta, \lambda < 0$ the identities of liquid and vapor phases are interchanged.) More specific mechanisms, due to hydrodynamics [24, 30] or chemotaxis [31, 32], have also been proposed to piecewise explain some of these phases. AMB+ does not refute such specific explanations but offers a minimal framework within which to address generic features of active phase equilibria. Its simplicity admits both significant analytical progress, and efficient numerics.

For active systems showing bulk liquid-vapor phase separation it has been debated, on the basis of numerical and analytical studies, how to define the liquid-vapor interfacial tension [33–39]. One of the key results of this Letter is to confirm that no unique definition is possible. Inspired by work on equilibrium interfaces [28], we derive an effective equation for the interface height, and calculate the capillary tension σ_{cw} which sets the spectrum of capillary waves and the relaxation times of height fluctuations. We find σ_{cw} differs from σ, the tension introduced

in [13] to describe the Ostwald process. Whereas $\sigma < 0$ in the reverse Ostwald regime, this does not ensure capillary instability, which instead requires $\sigma_{\mathrm{cw}} < 0$. When this holds, depending on the global density, we find two new types of active phase separation (Fig. 1), driven by an interfacial instability similar to that of Mullins and Sekerka [40]. We find both a microphase-separated droplet state, where coalescence among droplets is highly inhibited, and an 'active foam' state (Fig. 4).

As is standard [13, 26] we now set $M = 1$, assume constant D, K, and select $f(\phi) = a(-\phi^2/2 + \phi^4/4)$ with $a > 0$. (Our results can be extended to any double-well f and any $K(\phi) > 0$.) We present results for $\zeta > 0$, meaning that reversed Ostwald ripening happens only for vapor bubbles. The corresponding results for $\zeta < 0$ follow from the invariance of our model under $(\phi, \lambda, \zeta) \to -(\phi, \lambda, \zeta)$. We denote by ϕ_1 and ϕ_2 the coexisting vapor and liquid densities in the mean-field limit, $D = 0$; note that $\phi_{1,2} = \pm 1$ in the passive case only. More generally they are found by changing variables from ϕ and f to ψ and g (denoted 'pseudo-variables' [13]), which solve $K\partial^2\psi/\partial\phi^2 = (\zeta - 2\lambda)\partial\psi/\partial\phi$ and $\partial g/\partial\psi = \partial f/\partial\phi \equiv \mu$, whence $\psi = K\left(\exp[(\zeta - 2\lambda)\phi/K] - 1\right)/(\zeta - 2\lambda)$. In terms of them, the equilibrium conditions $\mu_1 = \mu_2$ and $(\mu\psi - g)_1 = (\mu\psi - g)_2$ still hold [13, 41]. All our analytic results are valid in dimensions $d \geq 2$, while our numerics were done in $d = 2$ with periodic boundary conditions and system size $L_x \times L_y$, using an efficient pseudo-spectral algorithm with Euler updating [42].
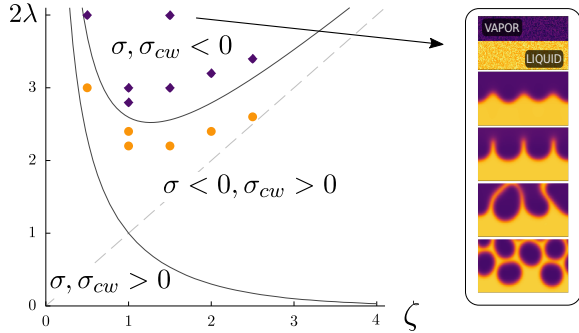

Figure 1. Mean-field phase diagram of AMB+ for $\zeta > 0$, showing sign regimes of interfacial tensions σ_{cw} and σ_{cw}. When $\sigma_{\mathrm{cw}} > 0$, the interface is stable and unstable otherwise. Orange circles and blue squares respectively denote the results of direct simulations of AMB+ where the instability of the interface is or is not observed. This shows the accuracy of our analytical prediction of the critical line $\sigma_{\mathrm{cw}} = 0$. Right: interfacial instability ($\zeta = 1.5, \lambda = 2$).

We start, following [29], by deriving the effective dynamics for the interface height $\hat{h}(\mathbf{x}, t)$ above a $(d - 1)$ plane, with in-plane and vertical coordinates $(\mathbf{x}, y) = \mathbf{r}$. We assume the absence of overhangs. On a rapid time-

scale, diffusion relaxes $\phi(\mathbf{r}, t)$ to a quasistatic profile that depend only on the distance to the interface which, for small amplitude, long-wavelength perturbations, can be measured along the y-direction:

$$\phi(\mathbf{r}, t) = \varphi(y - \hat{h}(\mathbf{x}, t)). \tag{4}$$

It will turn out that $\hat{h}$ solves a non-local equation in space, and we thus work in terms of its Fourier transform $h(\mathbf{q}_x, t)$. We proceed by plugging (4) into (1) and inverting the Laplace operator. We multiply $\nabla^{-2}\partial_t\varphi$ by $\partial_y\psi$, integrate across the interface, Fourier transform along the $\mathbf{x}$-direction, and expand in powers of h. Denoting $q = |\mathbf{q}_x|$, we obtain [42]

$$\partial_t h = -\frac{1}{\tau(q)}h + \chi + \mathcal{O}(h^2) \tag{5}$$

$$\frac{1}{\tau(q)} = \frac{2\sigma_{\mathrm{cw}}(q)q^3}{A(q)} \tag{6}$$

where

$$\sigma_{\mathrm{cw}}(q) = \sigma_\lambda + \frac{3\zeta}{4}\int dy_1 dy_2 \frac{(y_1 - y_2)}{|y_1 - y_2|}\frac{\psi'(y_1)\varphi'^2(y_2)}{e^{q|y_1 - y_2|}} \tag{7}$$

$$\sigma_\lambda = K\int dy\, \varphi'(y)\psi'(y) \tag{8}$$

and χ is a Gaussian noise of zero mean and correlations $\langle\chi(\mathbf{q}_1, t_1)\chi(\mathbf{q}_2, t_2)\rangle = C_\chi(q_1)\delta(\mathbf{q}_1 + \mathbf{q}_2)\delta(t_1 - t_2)$, with

$$C_\chi(q) = 4(2\pi)^{d-1}\frac{DB(q)}{A^2(q)}q. \tag{9}$$

In (6,9), $A(q) \equiv \int dy_1 dy_2\, \psi'(y_1)\varphi'(y_2)\exp(-q|y_1 - y_2|)$ and $B(q) \equiv \int dy_1 dy_2\, \psi'(y_1)\psi'(y_2)\exp(-q|y_1 - y_2|)$. Note that (5) omits nonlinear terms which are derived in [42]; these are essentially the same as studied in models of conserved surface roughening [43, 44].

The effective height equations (5-9) are the fundamental analytic results of this Letter. For wavelengths much larger than an interfacial width $\xi \sim (-K/a)^{1/2}$, we can replace $\sigma_{\mathrm{cw}}(q), A(q)$ and $B(q)$ with their limiting values as $q \to 0$. These, with a slight abuse of notation, are denoted as σ_{cw}, A and B. Explicitly, the resulting capillary-wave tension σ_{cw} obeys

$$\sigma_{\mathrm{cw}} = \sigma_\lambda - \frac{3\zeta}{2}\int dy\left[\psi(y) - \frac{\psi_1 + \psi_2}{2}\right]\varphi'^2(y) \tag{10}$$

where $\psi_{1,2} = \psi(\phi_{1,2})$ are the pseudo-densities at the binodals. As expected, σ_{cw} reduces to the standard interfacial tension, $\sigma_{\mathrm{eq}} = K\int dy\, \varphi'^2(y)$, in the equilibrium limit $\lambda, \zeta \to 0$ [45]. This governs not only the capillary fluctuation spectrum, but the Laplace pressure and the rate of Ostwald ripening [28, 29]. Switching on activity breaks this degeneracy. Indeed the tension determining the rate of Ostwald ripening of a bubble was given in [13] as $\sigma = \sigma_\lambda - \zeta\int dy\left[\psi - \psi(0)\right]\varphi'^2(y)$, where $\psi(0)$ is the value of the pseudo-density at the droplet center. Therefore $\sigma \neq \sigma_{\mathrm{cw}}$ in general.
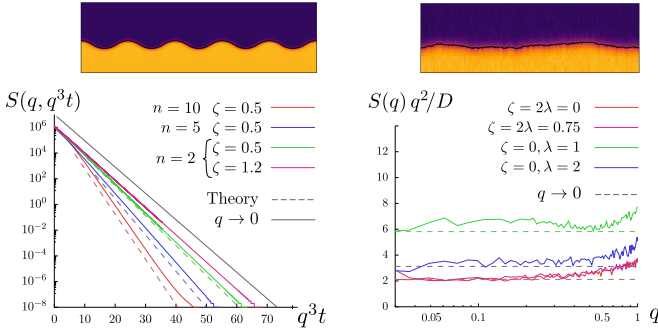
Figure 2. (Left) snapshot of the liquid-vapor interface in the regime $\sigma_{cw} > 0$ ($L_x = L_y = 256$) and the noiseless ($D = 0$, $\zeta = 2\lambda$) relaxation compared to the theoretical predictions for initial perturbations at wavenumber $2\pi n/L_x$. Dashed lines are predictions obtained using $\tau(q)$, converging to the $q \to 0$ limit (continuous line). (Right) snapshot in steady state for $D = 5 \times 10^{-3}$ and scaled structure factor $q^2 S(q)/D$ vs q compared to the $q \to 0$ analytical prediction; results are averaged over over 30 realisations of duration 10^6 after equilibration.

To obtain explicit predictions from (5-9), we need to evaluate σ_{cw}, A and B. This requires knowledge of the interfacial shape $\varphi(y)$. At equilibrium, this is well-known [45]: $\varphi_{eq}(y) = \pm\tanh(y/\xi_{eq})$ with $\xi_{eq} = \sqrt{2K/a}$ and $\sigma_{eq} = \sqrt{8Ka/9}$. (Note that $A = B = 4$ in this case.) Also, whenever $2\lambda = \zeta$ it is readily shown that $\varphi = \varphi_{eq}$ so that $\sigma_{cw} = \sigma_{eq}$, although the Ostwald tensions are $\sigma = \sigma_{eq}(1 \mp \zeta/K)$ for bubble growth ($-$) and liquid droplet growth ($+$) respectively [13]. We do not have closed-form results for σ_{cw} at general λ, ζ; however, a change of variable to $w(\varphi) = \varphi'^2$ in the integrals defining σ_{cw}, A, B allows use of a simple numerical procedure as first used in [21] and detailed in [42] to find the low q behavior. To examine $q \neq 0$ below we instead extract the interface profile from simulations at $D = 0$.

Fig. 1 shows a phase diagram of AMB+ for $\zeta > 0$ at mean-field level, delineating the zones of negative σ and σ_{cw}. (There are none at negative λ.) For small activity, or for $\lambda\zeta < 0$, $\sigma_{cw} > 0$, even where $\sigma < 0$; here vapor bubbles undergoing reversed Ostwald ripening have stable interfaces. But at high activity a new regime emerges where $\sigma_{cw} < 0$ implying that such interfaces (and also flat ones) become locally unstable.

We first consider the regime where $\sigma_{cw} > 0$, where our theory predicts this capillary tension to govern, via (6), the relaxation times of the interface $\tau(q)$. To check this, we performed simulations of AMB+ for $D = 0$ starting from a phase separated state with the interface perturbed via a single mode; Fig. 2 confirms that $h(\mathbf{q}, t) = h(\mathbf{q}, 0)\exp(-t/\tau(q))$ as predicted by (5-9), for either sign of the Ostwald tension σ. Our theory also predicts the stationary structure factor of the interface

$S(q) = \lim_{t\to\infty}\langle|h(\mathbf{q}, t)|^2\rangle$:

$$S(q) = \frac{(2\pi)^{d-1}D}{\sigma_{cw}(q)q^2}\frac{B(q)}{A(q)} \to_{q\xi^{-1}\ll 1} \frac{(2\pi)^{d-1}D_{eff}}{\sigma_{cw}q^2} \quad (11)$$

where $D_{eff} = D(\psi_2-\psi_1)/(\phi_2-\phi_1)$ is an effective capillary temperature. This result generalizes capillary wave theory. Its equilibrium analog, $S(q) \propto D/\sigma_{eq}q^2$ [46], is often justified using equipartition arguments but, even in equilibrium, higher order gradient terms give sub-leading corrections at finite q [47, 48]. Hence the hallmark of activity is not the similar corrections entering in (11); instead activity impacts the interfacial fluctuations by renormalizing the temperature $D \to D_{eff}$ and, separately, replacing σ_{eq} with σ_{cw}. Even though (11) also neglects the additional nonlinearities omitted from (5), it is quite accurate at small D (Fig. 2). The use of capillary wave theory in phase-separated active systems was previously advocated heuristically [34, 36, 37] but until now, only qualitative estimates were provided for the coefficient D_{eff}/σ_{cw} in (11).
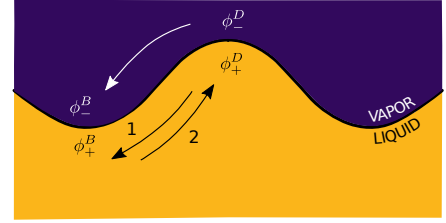

Figure 3. Mechanism of the interfacial instability when $\sigma_{cw} < 0$. The densities on the two sides of the interface adjust quasi-statically at values that depend on its local curvature, leading to diffusive density fluxes. That on the vapor side is always stabilising; that in the liquid becomes destabilising when $\sigma < 0$ (arrow 2). This (one-sided) reverse-Ostwald current does not trigger an instablity unless the current in the liquid outweighs that in the vapor, which requires $\sigma_{cw} < 0$.

We now turn to study the region where $\sigma_{cw} < 0$. Here a drastically new non-equilibrium phenomenology arises. Although the vapor–liquid interface is unstable to height fluctuations, we will see that the system remains phase separated. For, unlike in equilibrium where demixing itself cannot be sustained at negative tension, the active interface does not undergo diffusive collapse but remains stable against normal perturbations $\phi(\mathbf{x}, y) = \varphi(y) + \partial_y w(y)$. To see this, we linearize the mean-field dynamics around φ to obtain $\partial_t w = \mathcal{L}w$, where $\mathcal{L} = \partial_y\left[f''(\varphi) - K\partial_y^2 + (2\lambda - \zeta)\varphi'\partial_y\right]\partial_y$ and compute the spectrum of $\mathcal{L}$. In the equilibrium case, and thus also when $\zeta = 2\lambda$, this is continuous for an infinite system and it touches 0 [49, 50], resulting in algebraic decay of w in time. Extending this analysis to general ζ, λ lies beyond our scope. Instead we compute numerically the spectrum of $\mathcal{L}$ [42], concluding that the flat interface remains stable to normal perturbations irrespective of the
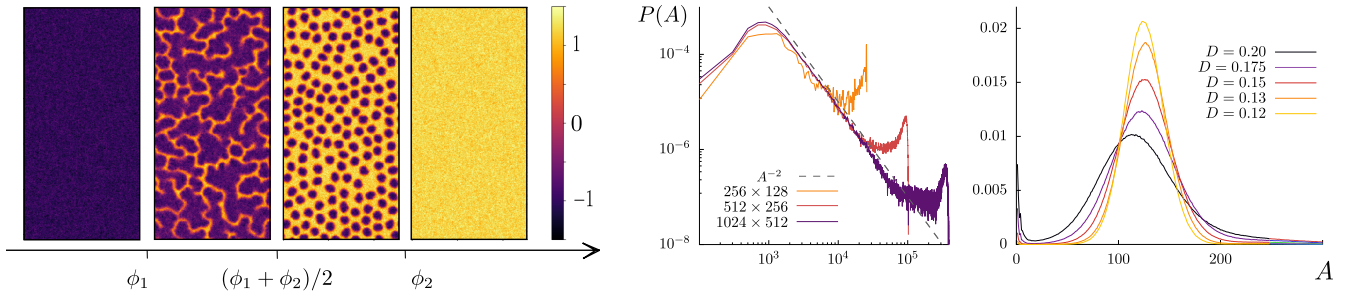
Figure 4. (Left) phase diagram when $\sigma_{cw} < 0$ as a function of the global density $\phi_0 = -1, -0.4, 0.4, 1.2$ at $D = 0.05, L_x = 256, L_y = 512$ and $\lambda = 1.75, \zeta = 2$, for which $\phi_1 = -0.9, \phi_2 = 1.08$. At high and low ϕ_0, the system is homogeneous (liquid or vapor states). Within the binodals, when the liquid is the majority phase, the system shows microphase-separated vapor bubbles whose coalescence is highly inhibited. At lower ϕ_0, the system forms a continuously evolving active foam state. (Middle and Right): area distribution of vapor regions for the active foam state ($\phi_0 = -0.4$) and in the microphase-separated state for the noise values in the legend ($\phi_0 = 0.2$).

sign of σ and σ_{cw}. Again the spectrum of $\mathcal{L}$ approaches 0 in the large-system limit, indicating algebraic decay of w.

Next, we numerically simulated AMB+ at $D = 0$, with a noisy initial condition. Orange and blue dots in Fig. 1 respectively represent cases where the interfacial fluctuation is damped or amplified (Movie 1), showing the accuracy of our analytical predictions. Computing $\tau(q)$ shows that the first unstable mode is at the lowest q available; thus the transition line $\sigma_{cw} = 0$ is critical [42].

The mechanism for the interfacial instability (Fig. 3) is reminiscent of the Mullins-Sekerka instability driving pattern formation in solidification [40]. In both cases the instability is driven by a single diffusing field: latent heat in crystal growth, and density in the present situation. Such a diffusing field settles to quasi-stationary values on the two sides of the interface which depend on the local curvature, with extrema denoted by $\phi_{\pm}^{B,D}$ in Fig. 3. By approximating $\phi_{\pm}^{B,D}$ as the densities near the interface of a vapor bubble (B) or liquid droplet (D), we find that the diffusive current on the vapor side is always stabilizing. In contrast, depending on whether Ostwald ripening is normal or reversed, the current on the liquid side is stabilizing or destabilizing. Reversed Ostwald ripening is however not sufficient to drive overall instability of the interface; this arises only if the current on the liquid side is stronger than the one on the vapor. This condition sets the threshold beyond which $\sigma_{cw} < 0$ and fluctuations grow. Measuring the steady state currents confirms this mechanistic picture to good accuracy [42].

We now report simulations with a small but finite noise level to ensures reproducible steady states. Starting from a near-uniform initial state, we find that the final phase separation is strongly affected by interfacial instability. The stable case, $\sigma_{cw} > 0$, was explored in [13]. For the unstable case, $\sigma_{cw} < 0$, the stationary states seen by varying the global density $\phi_0 = \int \phi d\mathbf{r}/V$ are reported in Fig. 4 and Movie 2. When ϕ_0 lies outside the mean-field

binodals $\phi_{1,2}$, the system remains homogeneous. Within them, at large ϕ_0 such that the liquid is the majority phase, we find a microphase-separated state where coalescence of crowded bubbles is highly inhibited. The bubble size distribution $P(A)$ is strongly peaked, the more peaked the lower the noise, suggesting that the average bubble size $\langle A \rangle$ is finite when $D \to 0$. Our results are converged in time for $D > 0.1$; at lower noise the system gets trapped into metastable states, evolving only because of rare fluctuations of the bubbles interface [42]. Understanding analytically the stability of circular bubbles would be key to compute $\langle A \rangle$ and $P(A)$. Clearly, though, the average size is not set by the most unstable mode of the flat interface, as the steady state is attained by a series of secondary instabilities (Movie 1 and 3). This phenomenology is at odds with the bubble phase at $\sigma_{cw} > 0$ [13], where a dynamical balance between nucleation, coalescence and reversed Ostwald causes $\langle A \rangle \to \infty$ when $D \to 0$. The difference between these two microphase separated states is also apparent in the dynamical evolution starting from bulk phase separation (Movie 3).

When the liquid is the minority phase, bubbles cannot avoid touching and coalescing. One might expect that the system attains a micro-phase separated state of liquid droplets (for $\zeta > 0$); this is not the case because, as is clear from our mechanistic argument above, the interfaces bends toward the vapor side. Instead, we find a previously unknown form of phase separation, which we call the 'active foam' state. Thin filaments of liquid are dispersed in the vapor phase, which continuously break up and reconnect. These filaments are bent on the most unstable length-scale of the flat interface, as if there were an underlying 'virtual packing' of polyhedral bubbles separated by thin films – but with many of these films absent. The area distribution of the vapor regions (Fig. 4b) is now peaked at at size that corresponds to the merging of two bubbles, but a power-law tail A^{-2} emerges, only

cut off by the system-size. Note that the boundaries in ϕ_0 between the different phases of Fig. 4 are qualitative: while the vapor density is almost independent of ϕ_0 the liquid density varies markedly [42].

The techniques introduced here could be used to elucidate the capillary tension in particle-based active models, by applying them to various field-theoretical descriptions obtained by explicit coarse-graining [13, 41, 51]. The roughening properties of the interface also merit further study: the anomalous scaling found in particle-based simulations was interpreted to be in the Edwards-Wilkinson universality class [36, 37]. Our linear theory, instead, gives the critical exponents $z = 3$ and $\chi = (z - d)/2$, but the impact of non-linearities should be studied by renormalisation.

Finally, although the reversal of the "Ostwald tension" σ was previously understood [13], it is remarkable that (a) the capillary tension can likewise become negative, and that (b) this leads to new types of phase separation including active foam states. Our approach is based on AMB+, whose generic, leading-order form is agnostic as to the microscopic mechanisms underlying activity (and even phase separation). This means that the microscopic ingredients needed for our new phases remain to be identified. For the exact same reason, we expect them to be widely present, not only in motility-induced phase separation [4], but in other phase-separating systems with locally broken detailed balance.

---

[1] S. Ramaswamy, J. Stat. Mech.: Theory Exp. **2017**, 054002 (2017).

[2] M. C. Marchetti, J. F. Joanny, S. Ramaswamy, T. B. Liverpool, J. Prost, M. Rao, and R. A. Simha, Rev. Mod. Phys. **85**, 1143 (2013).

[3] J. Tailleur and M. E. Cates, Phys. Rev. Lett. **100**, 218103 (2008).

[4] M. E. Cates and J. Tailleur, Annu. Rev. Condens. Matter Phys. **6**, 219 (2015).

[5] Y. Fily and M. C. Marchetti, Phys. Rev. Lett. **108**, 235702 (2012).

[6] T. Speck, J. Bialké, A. M. Menzel, and H. Löwen, Phys. Rev. Lett. **112**, 218304 (2014).

[7] E. Fodor, C. Nardini, M. E. Cates, J. Tailleur, P. Visco, and F. van Wijland, Phys. Rev. Lett. **117**, 038103 (2016).

[8] T. F. F. Farage, P. Krinninger, and J. M. Brader, Phys. Rev. E **91**, 042310 (2015).

[9] C. Maggi, U. Marini Bettolo Marconi, N. Gnan, and R. Di Leonardo, Sci. Rep. **5** (2015), 10.1038/srep10742.

[10] G. Szamel, Phys. Rev. E **93**, 012603 (2016).

[11] C. Nardini, E. Fodor, E. Tjhung, F. van Wijland, J. Tailleur, and M. E. Cates, Phys. Rev. X **7**, 021007 (2017).

[12] F. Caballero and M. E. Cates, Phys. Rev. Lett. **124**, 240604 (2020).

[13] E. Tjhung, C. Nardini, and M. E. Cates, Phys. Rev. X **8**, 031080 (2018).

[14] J. Stenhammar, D. Marenduzzo, R. J. Allen, and M. E. Cates, Soft Matter **10**, 1489 (2014).

[15] C. B. Caporusso, P. Digregorio, D. Levis, L. F. Cugliandolo, and G. Gonnella, Phys. Rev. Lett. **125**, 178004 (2020).

[16] X.-q. Shi, G. Fausti, H. Chaté, C. Nardini, and A. Solon, Phys. Rev. Lett. **125**, 168001 (2020).

[17] I. Theurkauff, C. Cottin-Bizonne, J. Palacci, C. Ybert, and L. Bocquet, Phys. Rev. Lett. **108**, 268303 (2012).

[18] I. Buttinoni, J. Bialké, F. Kümmel, H. Löwen, C. Bechinger, and T. Speck, Phys. Rev. Lett. **110**, 238301 (2013).

[19] S. Thutupalli, D. Geyer, R. Singh, R. Adhikari, and H. A. Stone, PNAS **115**, 5403 (2018).

[20] E. Demir, Y. I. Yaman, M. Basaran, and A. Kocabas, Elife **9**, e52781 (2020).

[21] R. Wittkowski, A. Tiribocchi, J. Stenhammar, R. J. Allen, D. Marenduzzo, and M. E. Cates, Nat. Comms. **5** (2014).

[22] F. J. Thomsen, L. Rapp, F. Bergmann, and W. Zimmermann, New J. Phys. (2021).

[23] A. Tiribocchi, R. Wittkowski, D. Marenduzzo, and M. E. Cates, Phys. Rev. Lett. **115**, 188302 (2015).

[24] R. Singh and M. E. Cates, Phys. Rev. Lett. **123**, 148005 (2019).

[25] E. Tjhung, D. Marenduzzo, and M. E. Cates, PNAS **109**, 12381 (2012).

[26] P. C. Hohenberg and B. I. Halperin, Rev. Mod. Phys. **49**, 435 (1977).

[27] P. M. Chaikin and T. C. Lubensky, *Principles of condensed matter physics*, Vol. 1 (Cambridge Univ Press, 2000).

[28] A. J. Bray, A. Cavagna, and R. Travasso, Phys. Rev. E **65**, 016104 (2001).

[29] A. J. Bray, Adv. Phys. **51**, 481 (2002).

[30] R. Matas-Navarro, R. Golestanian, T. B. Liverpool, and S. M. Fielding, Phys. Rev. E **90**, 032304 (2014).

[31] B. Liebchen, D. Marenduzzo, I. Pagonabarraga, and M. E. Cates, Phys. Rev. Lett. **115**, 258301 (2015).

[32] S. Saha, R. Golestanian, and S. Ramaswamy, Phys. Rev. E **89**, 062316 (2014).

[33] A. P. Solon, J. Stenhammar, M. E. Cates, Y. Kafri, and J. Tailleur, New J. Phys. **20**, 075001 (2018).

[34] J. Bialké, J. T. Siebert, H. Löwen, and T. Speck, Phys. Rev. Lett. **115**, 098301 (2015).

[35] R. Zakine, Y. Zhao, M. Knežević, A. Daerr, Y. Kafri, J. Tailleur, and F. van Wijland, Phys. Rev. Lett. **124**,

248003 (2020).

[36] C. F. Lee, Soft matter **13**, 376 (2017).

[37] A. Patch, D. M. Sussman, D. Yllanes, and M. C. Marchetti, Soft matter **14**, 7435 (2018).

[38] A. K. Omar, Z.-G. Wang, and J. F. Brady, Phys. Rev. E **101**, 012604 (2020).

[39] S. Hermann, D. de las Heras, and M. Schmidt, Phys. Rev. Lett. **123**, 268002 (2019).

[40] J. S. Langer, Rev. Mod. Phys. **52**, 1 (1980).

[41] A. P. Solon, J. Stenhammar, M. E. Cates, Y. Kafri, and J. Tailleur, Phys. Rev. E **97**, 020602 (2018).

[42] See Supplemental Material at [URL will be inserted by publisher].

[43] F. Caballero, C. Nardini, F. van Wijland, and M. E. Cates, Phys. Rev. Lett. **121**, 020601 (2018).

[44] T. Sun, H. Guo, and M. Grant, Phys. Rev. A **40**, 6763 (1989).

[45] M. E. Cates and E. Tjhung, J. Fluid Mech. **836**, P1 (2018).

[46] J. S. Rowlinson and B. Widom, *Molecular theory of capillarity* (Courier Corporation, 2013).

[47] J. Meunier, J. Phys. **48**, 1819 (1987).

[48] E. M. Blokhuis and D. Bedeaux, Mol. Phys. **80**, 705 (1993).

[49] A. Shinozaki and Y. Oono, Phys. Rev. E **47**, 804 (1993).

[50] J. Bricmont, A. Kupiainen, and J. Taskinen, Commun. Pure Appl. Math. **52**, 839 (1999).

[51] J. Bickmann and R. Wittkowski, Phys. Rev. Res. **2**, 033241 (2020).

G. Fausti,[1] E. Tjhung,[2] M. E. Cates,[3] and C. Nardini[1,4]

[1] *Service de Physique de l'Etat Condensé, CEA, CNRS Université Paris-Saclay, CEA-Saclay, 91191 Gif-sur-Yvette, France*
[2] *Department of Physics, University of Durham, Science Laboratories, South Road, Durham DH1 3LE, UK*
[3] *DAMTP, Centre for Mathematical Sciences, University of Cambridge, Wilberforce Road, Cambridge CB3 0WA, UK*
[4] *Sorbonne Université, CNRS, Laboratoire de Physique Théorique de la Matière Condensée, 75005 Paris, France*
(Dated: June 8, 2021)

Appendix A: Details on the numerical analysis

We integrated AMB+ with a parallel pseudo-spectral code employing periodic boundary conditions and Euler time-update. In all our simulations we set $K = 1$, $a = 1/4$, spatial spatial discretisation $\Delta x = 1$, time-step $dt = 2 \times 10^{-2}$; we checked that our results are stable upon decreasing Δx and dt.

1. Identification of the interface

To locate the interface, for every x coordinate, we find the first pixel $\bar{y}$ such $\phi(x, \bar{y}) > \phi_{th}$. We then place the interface at

$$h(x) = \bar{y} + \frac{\phi(x, \bar{y}) - \phi_{th}}{\phi(x, \bar{y}) - \phi(x, \bar{y} + \Delta x)} \tag{A1}$$

where $\phi_{th} = (\phi_1 + \phi_2)/2$. Different values of ϕ_{th} do not change the results as far as ϕ_{th} is sufficiently far from the binodals.

2. Measure of the bubble-size distribution

To measure the distribution of bubbles area, we first transformed the density field in a binary matrix using the threshold ϕ_{th}. Scanning this matrix sequentially, we then applied a breadth-first search algorithm; the outcome is an $L_x \times L_y$ matrix where each pixel is labeled accordingly to the cluster it belongs to. Building the pdf of the vapor regions is then straghtforward. The analysis was performed on a smoothened density field obtained by running a few time-steps of the dynamics without noise.

Appendix B: Effective interface equation in the mean-field approximation

In this Appendix we detail the derivation of the effective interface equation (5) of the main text. We start from the mean-field problem ($D = 0$) in Appendix B 1 and consider the effect of noise in Appendix B 2. We also obtain the leading non-linear terms, of order $\mathcal{O}(h^2)$, that correct eq. (5).

The full, non-linear, effective equation for h that we obtain is

$$\partial_t h = -\frac{2\sigma_{cw}(q)q^3}{A(q)}h + \zeta\frac{C(q)}{A(q)}\Big\{ -q^2\mathcal{F}\Big[|\nabla_{\mathbf{x}}\hat{h}|^2\Big]$$
$$+ \mathcal{F}\Big[\nabla_{\mathbf{x}} \cdot (\nabla_{\mathbf{x}}^2\hat{h}\nabla_{\mathbf{x}}\hat{h})\Big]\Big\} + \chi + \mathcal{O}(\zeta h^3) \tag{B1}$$

where $\mathcal{F}[\cdot]$ is the Fourier transform operator along the $\mathbf{x}$ direction, and

$$C(q) = \int dy_1 dy_2\, \psi'(y_1)\varphi'^2(y_2)e^{-q|y_1 - y_2|}. \tag{B2}$$

The other quantities appearing in (B1) were defined in the main text and are reported here for convenience:

$$\sigma_{cw}(q) = \sigma_\lambda + \frac{3\zeta}{4}\int dy_1 dy_2\, \frac{(y_1 - y_2)}{|y_1 - y_2|}\frac{\psi'(y_1)\varphi'^2(y_2)}{e^{q|y_1 - y_2|}}$$

$$\sigma_\lambda = K\int dy\, \varphi'(y)\psi'(y) \tag{B3}$$

$$A(q) = \int dy_1 dy_2\, \psi'(y_1)\varphi'(y_2)\exp\left(-q|y_1 - y_2|\right) \tag{B4}$$

$$B(q) = \int dy_1 dy_2\, \psi'(y_1)\psi'(y_2)\exp(-q|y_1 - y_2|). \tag{B5}$$

Finally, the noise χ is Gaussian and has correlations $\langle \chi(\mathbf{q}_1, t_1)\chi(\mathbf{q}_2, t_2)\rangle = C_\chi(q_1)\delta(\mathbf{q}_1 + \mathbf{q}_2)\delta(t_1 - t_2)$, where

$$C_\chi(q) = 4(2\pi)^{d-1}\frac{DB(q)}{A^2(q)}q. \tag{B6}$$

1. Effective interface equation for D=0

Assuming

$$\phi(\mathbf{r}, t) = \varphi(y - \hat{h}(\mathbf{x}, t)) \tag{B7}$$

in the AMB+ dynamics, we obtain

$$\nabla^{-2}\partial_t\varphi = f'(\varphi) - K\nabla^2\varphi + \lambda|\nabla\varphi|^2$$
$$- \zeta\nabla^{-2}\nabla \cdot \left[(\nabla^2\varphi)\nabla\varphi\right] \tag{B8}$$

where $\hat{g}(\mathbf{x}, y) = \nabla^{-2}\hat{s}(\mathbf{x}, y)$ means that $\hat{g}$ solves $\nabla^2\hat{g} = \hat{s}$. It is easy to show that the Fourier transform of $\hat{g}$ along $\mathbf{x}$ is given by

$$g(\mathbf{q}, y) = -\frac{1}{2q}\int dy_1 e^{-q|y - y_1|}s(\mathbf{q}, y_1). \tag{B9}$$

Let us first consider the equilibrium case $\lambda = \zeta = 0$, hence generalizing the approach of [1] to arbitrary q-values. Applying the chain rule to (B8) gives

$$-\nabla^{-2}\left[\varphi'\partial_t\hat{h}\right] = \tag{B10}$$
$$f'(\varphi) - K\varphi''(1 + |\nabla_{\mathbf{x}}\hat{h}|^2) + K\varphi'\nabla_{\mathbf{x}}^2\hat{h}$$

where $\nabla_{\mathbf{x}}$ is the gradient with respect to $\mathbf{x}$. We then multiply by φ' and integrate over $u = y - \hat{h}(\mathbf{x}, t)$ across the interface to get

$$-\int du\,\varphi'(u)\nabla^{-2}\left[\varphi'(u)\partial_t\hat{h}\right] = \Delta f + \sigma_{eq}\nabla_{\mathbf{x}}^2\hat{h} \tag{B11}$$

where $\Delta f = f(\phi_2) - f(\phi_1)$, we have assumed that $\phi(y \to \infty) = \phi_2$ and $\phi(y \to -\infty) = \phi_1$, and that φ' vanishes in the bulk. Fourier transforming along the $\mathbf{x}$ direction and using (B9) gives

$$\partial_t h = -\frac{2\sigma_{eq}q^3}{A_{eq}(q)}h \tag{B12}$$

where $A_{eq}(q) = \int dy_1 dy_2\,\varphi'(y_1)\varphi'(y_2)\exp\left(-q|y_1 - y_2|\right)$. Observe that the term coming from Δf in (B11) is proportional to $q\delta(\mathbf{q})$ and thus vanishes. Eq. (B12) is the deterministic part of the effective interface equation for Model B.

We now consider $\lambda, \zeta \neq 0$. From (B8), the analog to (B10) now reads

$$-\nabla^{-2}\left[\varphi'(u)\partial_t\hat{h}\right] = \mu_\lambda + \mu_\zeta \tag{B13}$$

where

$$\mu_\lambda = f'(\varphi) + (1 + |\nabla_{\mathbf{x}}\hat{h}|^2)(\lambda\varphi'^2 - K\varphi'') + K\varphi'\nabla_{\mathbf{x}}^2\hat{h}$$
$$\mu_\zeta = -\zeta\nabla^{-2}\left\{\nabla_{\mathbf{x}}\cdot\left[\left(\varphi''|\nabla_{\mathbf{x}}\hat{h}|^2 - \varphi'\nabla_{\mathbf{x}}^2\hat{h} + \varphi''\right)\right.\right. \tag{B14}$$
$$\left.\left(-\varphi'\nabla_{\mathbf{x}}\hat{h}\right)\right] + \partial_y\left[\left(\varphi''|\nabla_{\mathbf{x}}\hat{h}|^2 - \varphi'\nabla_{\mathbf{x}}^2\hat{h} + \varphi''\right)\varphi'\right]\right\}.$$

In order to progress we need to introduce the pseudo-variables [2] ψ, g, defined as the solution to

$$\frac{\partial^2\psi}{\partial\phi^2} = \frac{\zeta - 2\lambda}{K}\frac{\partial\psi}{\partial\phi} \quad\text{and}\quad \frac{\partial g}{\partial\psi} = \frac{\partial f}{\partial\phi} \tag{B15}$$

such that $\psi \to \phi$ and $g(\phi) \to f(\phi)$ in the passive limit ($\lambda \to 0$ and $\zeta \to 0$). These quantities play the same technical role as the one played by the density ϕ and by the local free energy f in equilibrium systems for computing the binodals [2, 3] or for computing the surface tension σ [2], although they lack the analogous physical interpretation.

We then multiply (B13) by ψ', integrate across the interface and apply the Fourier transform along $\mathbf{x}$. For the left hand side of (B13) we obtain

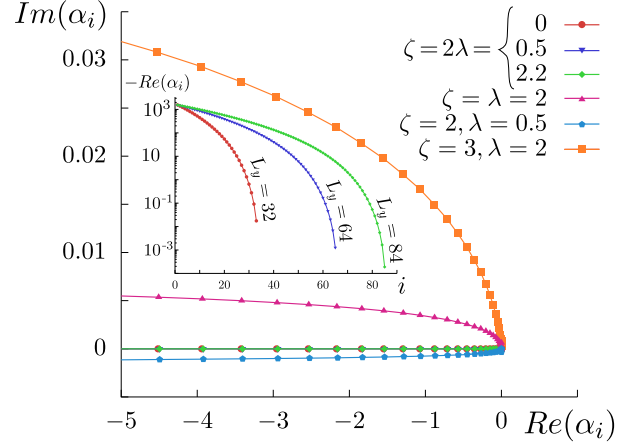$$\frac{A(q)}{2q}\partial_t h(\mathbf{q}, t) \tag{B16}$$

Figure 1. Spectrum of $\mathcal{L}(q_1 - q_2)$ for a system of linear size $L_y = 128$, spatial discretization $\Delta x = 1$ and values of the parameters as in the legend. The continuous lines are our estimate of the continuous spectrum of $\mathcal{L}(q_1 - q_2)$ in the infinite system-size limit. Although the spectrum is modified with respect to the equilibrium case, its crucial properties are not: all eigenvalues are negative and touch 0 in the infinite system-size limit implying that the vapor-liquid interface is stable to normal perturbations but disturbances will only decay algebraically in time.

where $A(q)$ is given in the main text and in (B4).

Concerning the right hand side of (B13), the first term in μ_λ becomes

$$\delta(\mathbf{q})\int_{-\infty}^{\infty} du\,\psi'(u)f'(\varphi) = g(\psi_2) - g(\psi_1) = 0$$

where we used the definition of g. To evaluate the second term in μ_λ we observe that

$$\int_{-\infty}^{\infty} du\,(\lambda\varphi'^2(u) - K\varphi''(u))\psi'(u)$$
$$= \frac{\zeta}{2}\int_{-\infty}^{\infty} du\,\varphi'^2(u)\psi'(u) \tag{B17}$$

where we have used (B15). The contribution in (B17) will be cancelled by an opposite one coming from μ_ζ. The third term in μ_λ gives

$$-q^2\sigma_\lambda h(\mathbf{q}, t) \tag{B18}$$

where σ_λ is defined in (B3).

We now consider μ_ζ in (B14). Expanding in powers of $\hat{h}$, we have

$$\nabla_{\mathbf{x}}^2\left(\frac{1}{\zeta}\mu_\zeta\right) = -\frac{1}{2}\partial_y^2(\varphi'^2) + \frac{3}{2}\partial_y(\varphi'^2)\nabla_{\mathbf{x}}^2\hat{h} \tag{B19}$$
$$-\varphi'^2\nabla_{\mathbf{x}}\cdot[\nabla_{\mathbf{x}}^2 h\nabla_{\mathbf{x}}\hat{h}] - \partial_y^2(\varphi'^2)|\nabla_{\mathbf{x}}\hat{h}|^2 + \mathcal{O}(\zeta h^3).$$

We then invert the Laplacian using (B9) and use

$$\partial_u e^{-q|y-u|} = q\,\text{sgn}(y-u)e^{-q|y-u|} \tag{B20}$$

where sgn is the sign function. Applying the same procedure as before and adding up the result with (B16), (B17), (B18) we obtain the deterministic part of (B1).
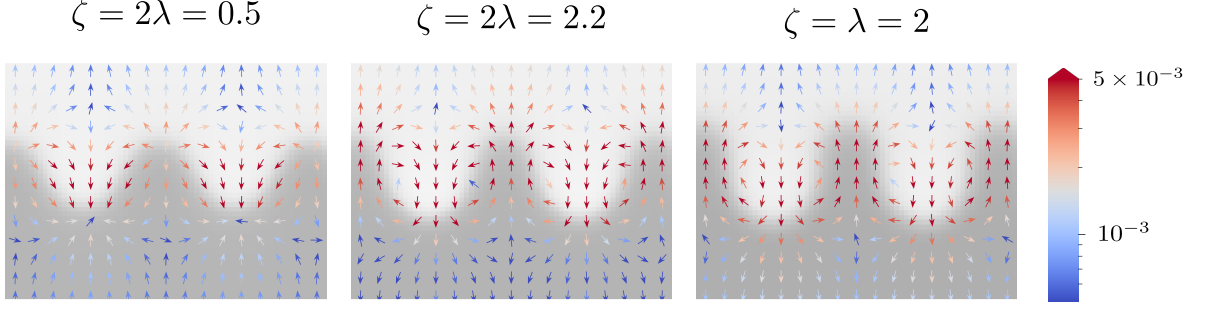
$$\zeta = 2\lambda = 0.5 \qquad \zeta = 2\lambda = 2.2 \qquad \zeta = \lambda = 2$$

Figure 2. Current $\mathbf{J}$ close to (left) the stable interface and normal Ostwald ripening ($\zeta = 2\lambda = 0.5$), (middle) stable interface and reversed Ostwald ripening for bubbles ($\zeta = 2\lambda = 2.2$) and (right) unstable interface ($\zeta = \lambda = 2$). Simulations are at mean-field ($D = 0$). The liquid is shown in dark gray and the magnitude of the current in colors. Only a small part of the system is shown. We measured $\bar{J}_V - \bar{J}_L = 0.04$ for $2\lambda = \zeta = 0.5$, $\bar{J}_V - \bar{J}_L = 0.08$ for $2\lambda = \zeta = 2.2$ and $\bar{J}_V - \bar{J}_L = -0.02$ for $2\lambda = \zeta = 2$. This confirms that the instability arises only when the current on the liquid side overwhelms the one on the vapor side.

2. Effect of $D \neq 0$

We now consider $D \neq 0$. Our goal is twofold: first, we derive the noise χ that enters in the effective interface equation (B1); second, we show that the Ito term that might correct (B1) actually vanishes. We start from this latter point by rewriting (B7) as

$$\phi(\mathbf{r}, t) = \varphi\left(y - \frac{1}{(2\pi)^{d-1}}\int d\mathbf{q}\, h(\mathbf{q}, t)e^{i\mathbf{q}\cdot\mathbf{x}}\right). \quad (B21)$$

The time derivative of ϕ gives

$$\partial_t\phi = -\varphi'\partial_t\hat{h} + \frac{1}{(2\pi)^{2(d-1)}}\varphi''\int d\mathbf{q}_1 d\mathbf{q}_2\, e^{i(\mathbf{q}_1+\mathbf{q}_2)\cdot\mathbf{x}}$$
$$2Dq_1\frac{B(q_1)}{A^2(q_1)}\delta(\mathbf{q}_1 + \mathbf{q}_2) \quad (B22)$$

and hence

$$\partial_t\phi = -\varphi'\partial_t\hat{h} + \frac{2D}{(2\pi)^{2(d-1)}}\varphi''\int d\mathbf{q}\, q\frac{B(q)}{A^2(q)} \quad (B23)$$

where last term in (B23) is the Ito contribution. It is then easy to show that this term gives a contribution proportional to $q\delta(q)$ in $\partial_t h$, and hence vanishes.

We are left with deriving the noise χ and show that its correlation is given by (B6). We first consider

$$\xi(\mathbf{x}, y, t) = (\nabla^{-2}\eta)(\mathbf{x}, y, t) \quad (B24)$$

where $\eta = -\nabla \cdot \sqrt{2D}\mathbf{\Lambda}$. Being a linear transformation of η, ξ is also a Gaussian noise. Its correlation reads

$$C_\xi(\mathbf{x}, y, t) = -2D\nabla^{-2}\delta(\mathbf{x})\delta(y)\delta(t) \quad (B25)$$

and its Fourier transform along $\mathbf{x}$

$$C_\xi(q, y, t) = \frac{D}{q}e^{-q|y|}\delta(t) \quad (B26)$$

where we have used (B9). The noise χ is given by

$$\chi(\mathbf{q}, t) = \frac{2q}{A(q)}\mathcal{F}\left[\int du\,\psi'(u)\xi(\mathbf{x}, u + \hat{h}(\mathbf{x}, t), t)\right](\mathbf{q}, t)$$

which is also Gaussian. It is now straightforward to show that the correlation of χ is given by (B6). This concludes the derivation of the effective interface equation (B1).
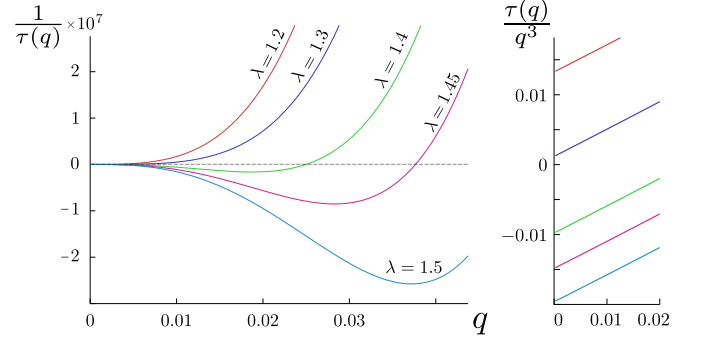

Figure 3. Damping rate $1/\tau(q)$ vs q at $\zeta = 1$ crossing the stability line. The instability arises at $q = 0$ in an infinite system: this is in fact the first mode whose damping rate becomes negative.

Appendix C: Profile φ of the flat interface

As reported in the main text, the flat interfacial profile $\varphi(y)$ can be found analytically only for the case $2\lambda = \zeta$, where it equals the equilibrium case. For generic values of λ, ζ, however, $w(\phi) = \varphi'^2$ can be obtained with a very simple numerical procedure using a technique introduced in [4] and then applied to AMB+ in [2]. We report it here for completeness.

First, as shown in [2], the binodals are easily obtained numerically solving $\mu = f'(\phi_1) = f'(\phi_2)$ and $\mu\psi_1 - g(\phi_1) = \mu\psi_2 - g(\phi_2)$. It is then easy to show that w solves

$$Kw' = (2\lambda - \zeta)w = 2(f' - \mu) \quad (C1)$$

which is solved by

$$w(x) = e^{-\frac{\zeta - 2\lambda}{K}x}\left[c + \frac{2}{K}\int_1^x e^{\frac{\zeta-2\lambda}{K}y}(f'(x) - \mu)dy\right](\text{C2})$$

The knowledge of $\phi_{1,2}$ allows to fix the integration constant c and the numerical evaluation of w via (C2) is straightforward.
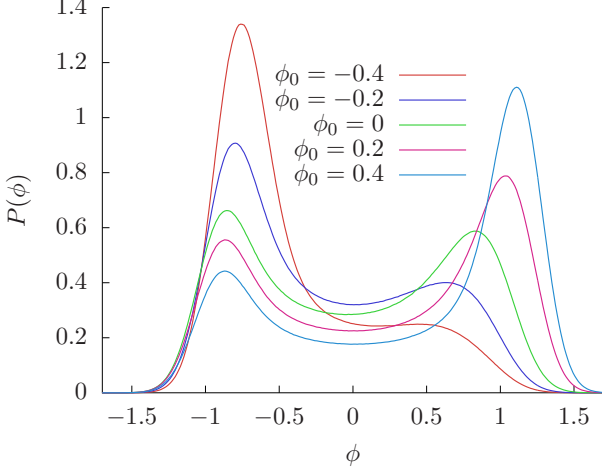

Figure 4. PDF of the density for $\zeta = 2$, $\lambda = 1.75$, $D = 0.05$ in a system 128×256 and several global densities ϕ_0 reported in the legend.

Appendix D: Stability against normal perturbations

We study here the linear stability to normal perturbations of the flat interface φ at mean-field level ($D = 0$). Due to mass conservation, the perturbed interface can be written as

$$\phi(\mathbf{x}, y, t) = \varphi(y) + \partial_y w(y, t) \qquad (\text{D1})$$

where φ solves

$$\partial_y^2\left[f''(\varphi) - K\partial_y^2\varphi + (\lambda - \zeta/2)\varphi'^2\right] = 0. \qquad (\text{D2})$$

Hence w satisfies

$$\partial_t w = \mathcal{L}w + \mathcal{O}(w^2) \qquad (\text{D3})$$

where the linear operator $\mathcal{L}$ is

$$\mathcal{L} = \partial_y\left[f''(\varphi) - K\partial_y^2 + (2\lambda - \zeta)\varphi'\partial_y\right]\partial_y. \qquad (\text{D4})$$

We are thus led to study the spectrum of $\mathcal{L}$. In equilibrium, this problem is tractable analytically because $\mathcal{L}$ is self-adjoint. It was found [5, 6] that the spectrum of $\mathcal{L}$ is continuous and touches 0 in an infinite system (it is in fact $(-\infty, 0)$), implying that the decay of w in time is algebraic in an infinite system. From (D4) we see that the same result applies for $2\lambda = \zeta$.

For generic λ and ζ, we studied numerically the spectrum of $\mathcal{L}$ for finite systems. By Fourier transforming along y, and for the choice of a double well local free energy f, the kernel of $\mathcal{L}$ is given by

$$\mathcal{L}(q_1 - q_2) = (-Kq_1^4 + Aq^2)\delta(q_1 - q_2) \qquad (\text{D5})$$
$$- 3Aq_1q_2\mathcal{F}_y[\varphi^2](q_1 - q_2)$$
$$+ (2\lambda - \zeta)q_1q_2^2(q_1 - q_2)\mathcal{F}_y[\varphi](q_1 - q_2)$$

where $\mathcal{F}_y[\cdot]$ denotes the Fourier transform operator along y. We discretised this operator on a grid with discretization step $\Delta x = 1$, total length L_y, and computed numerically the spectrum for several values of λ, ζ. Some of our results are reported in Fig. 1, showing that the qualitative picture is the same as at equilibrium: the spectrum is expected to be continuous and to touch 0 for an infinite system. It should be observed that these conclusions apply irrespectively of the sign of both σ and σ_{cw}: in both cases, φ is stable against normal perturbations.
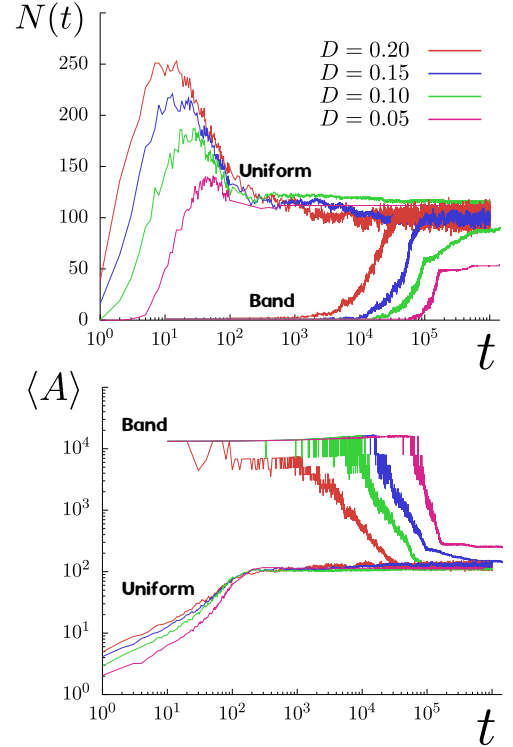

Figure 5. Evolution in time of the average bubble size $\langle A\rangle$ and of their number N_b for $\zeta = 2, \lambda = 1.75$ and various noise values starting either from an uniform or a fully phase separated state with a flat interface.

Appendix E: Instability against height perturbations ($\sigma_{cw} < 0$)

In the main text, we have discussed the analogy between the instability of the flat interface taking place

when $\sigma_{cw} < 0$ and the Mullins-Sekerka instability [7]. In Fig. 2 we further support this mechanistic picture, plotting the quasi-static current close to the perturbed interface. We consider three sets of parameter values corresponding to normal Ostwald ripening ($\sigma > 0$), reversed Ostwald ripening but stable interface ($\sigma < 0$, $\sigma_{cw} > 0$), and unstable interface ($\sigma < 0, \sigma_{cw} < 0$). The current on the vapor side is always stabilizing while it is stabilizing in the liquid side only if $\sigma > 0$. However, $\sigma < 0$ is not sufficient to drive the instability. For this, the destabilizing current on the liquid side needs to be stronger than the one on the vapor side. This happens only in the rightmost case of Fig. 2, which corresponds to $\sigma_{cw} < 0$. To show this, we have measured the average current $\bar{J}_V$ in the liquid projected along $e_{\mathbf{x}} = \mathbf{x}/|\mathbf{x}|$ defined as

$$\bar{J}_L^2 = \int dx \int_{\{y|\phi(\mathbf{x},y,t)>\phi_{th}\}} dy(\mathbf{J} \cdot e_{\mathbf{x}})^2 \qquad \text{(E1)}$$

and the analogous quantity in the vapor $\bar{J}_V$.

We further show that the instability of the flat interface is critical, i.e. the most unstable mode is the smallest available one ($q = 0$ in an infinite system). To show this we leveraged on the fact that we have an analytic expression, eq. (6) of the main text, for the damping rate $1/\tau(q)$ in the effective interface equation. From simulations at $D = 0$ and system-size $L_x = L_y = 256$ we extracted the interfacial profile $\varphi(y)$ and then used it to evaluate $\tau(q)$ at arbitrarily low q. The results for $\zeta = 1$ and varying λ are reported in Fig. 3.

Appendix F: Liquid and vapor densities in the microphase separated and active foam states

In Fig. 4, we report the PDF of the density as a function of the global density ϕ_0. The vapor density is found, to a good accuracy, independent of ϕ_0. Instead, the liquid density varies rather significantly with ϕ_0. This is expected because of two reasons: the liquid density with which a finite size vapor bubble is in equilibrium differs from the binodal [2] and the presence of multiple droplets further change such value. Obtaining the dependence of the liquid density on ϕ_0 is an open problem.

Appendix G: Evolution towards the microphase separated state

In Fig. 5 we plot the evolution, starting from an homogeneous state or a fully phase separated state, of the average size of bubbles and their number while converging to the microphase separated state. As shown, the convergence slows down when decreasing the noise value. This is because the initially formed bubbles are stable to small perturbations of their interface and evolution to the steady state is possible only by rare events at low noise.

Appendix H: Movies

- Movie 1 : Interfacial instability starting from a fully phase separated initial condition with noise added in the bulk. Parameters: $D = 0, \zeta = 2.25, \lambda = 1.8$. System size $L_x = L_y = 128$. Total density $\phi_0 = 0.2$, leading to a microphase separation in the steady state.

- Movie 2 : Phase diagram for $D = 0.05, \zeta = 2, \lambda = 1.75$ as a function of the density, showing the dynamics in the microphase separated and in the active foam state. System size $2L_x = L_y = 256$.

- Movie 3 : Evolution from a phase separated initial condition for $\zeta = 1.5, \lambda = 2.5, D = 0.1$, which corresponds to $\sigma_{cw} < 0$, and for $\zeta = 2\lambda = 2.2, D = 0.25$, which corresponds to $\sigma_{cw} > 0$. This show the markedly different evolution towards the microphase separated states found at $\sigma_{cw} < 0$ and at $\sigma_{cw} > 0$. Total simulation time is 10^6 and system size $L_x = L_y = 400$.

[1] A. J. Bray, A. Cavagna, and R. Travasso, Phys. Rev. E **65**, 016104 (2001).
[2] E. Tjhung, C. Nardini, and M. E. Cates, Phys. Rev. X **8**, 031080 (2018).
[3] A. P. Solon, J. Stenhammar, M. E. Cates, Y. Kafri, and J. Tailleur, Phys. Rev. E **97**, 020602 (2018).
[4] R. Wittkowski, A. Tiribocchi, J. Stenhammar, R. J. Allen, D. Marenduzzo, and M. E. Cates, Nat. Comms. **5** (2014).
[5] A. Shinozaki and Y. Oono, Phys. Rev. E **47**, 804 (1993).
[6] J. Bricmont, A. Kupiainen, and J. Taskinen, Commun. Pure Appl. Math. **52**, 839 (1999).
[7] J. S. Langer, Rev. Mod. Phys. **52**, 1 (1980).